THE ASTROPHYSICAL JOURNAL, 429:4–21, 1994 July 1

X-RAY CLUSTERS IN A COLD DARK MATTER + Λ UNIVERSE: A DIRECT, LARGE-SCALE, HIGH-RESOLUTION, HYDRODYNAMIC SIMULATION

RENYUE CEN AND JEREMIAH P. OSTRIKER
Princeton University Observatory, Princeton, NJ 08544
Received 1993 October 4; accepted 1993 December 30

ABSTRACT

A new, three-dimensional, shock-capturing, hydrodynamic code is utilized to determine the distribution of hot gas in a CDM + Λ model universe. Periodic boundary conditions are assumed: a box with size 85 h^{-1} Mpc, having cell size 0.31 h^{-1} Mpc, is followed in a simulation with $270^3 = 10^{7.3}$ cells. We adopt $\Omega = 0.45$, $\lambda = 0.55$, $h \equiv H/100$ km s^{-1} Mpc$^{-1} = 0.6$, and then, from *COBE* and light element nucleosynthesis, $\sigma_8 = 0.77$, $\Omega_b = 0.043$. We identify the X-ray emitting clusters in the simulation box, compute the luminosity function at several wavelength bands, the temperature function and estimated sizes, as well as the evolution of these quantities with redshift. This open model succeeds in matching local observations of clusters in contrast to the standard $\Omega = 1$, CDM model, which fails. It predicts an order of magnitude decline in the number density of bright ($h\nu = 2$–10 keV) clusters from $z = 0$ to $z = 2$ in contrast to a slight increase in the number density for standard $\Omega = 1$, CDM model.

This *COBE*-normalized CDM + Λ model produces approximately the same number of X-ray clusters having $L_x > 10^{43}$ ergs s^{-1} as observed. The background radiation field at 1 keV due to clusters is ~10% of the observed background which, after correction for numerical effects, again indicates that the model is consistent with observations.

The number density of bright clusters increases to $z \sim 0.2$–0.5 and then declines, but the luminosity per typical cluster decreases monotonically with redshift, with the result that the number density of bright clusters shows a broad peak near $z = 0.5$, and then a rapid decline as $z \to 3$. The most interesting point which we find is that the temperatures of clusters in this model freeze out at later times ($z \lesssim 0.3$), while previously we found in the CDM model that there was a steep increase during the same interval of redshift. Equivalently, we find that L^* of the Schechter fits of cluster luminosity functions peaks near $z = 0.3$ in this model, while in the CDM model it is a monotonically decreasing function of redshift. Both trends should be detectable even with a relatively "soft" X-ray instrument such as *ROSAT*, providing a powerful discriminant between $\Omega = 1$ and $\Omega < 1$ models. Detailed computations of the luminosity functions in the range $L_x = 10^{40}$–10^{44} ergs s^{-1} in various energy bands are presented for both cluster cores ($r \lesssim 0.5\ h^{-1}$ Mpc) and total luminosities ($r < 1\ h^{-1}$ Mpc). These are to be used for comparison with *ROSAT* and other observational data sets. They show the above noted negative evolution.

We find little dependence of core radius on cluster luminosity and the dependence of temperature on luminosity $\log kT_x = A + B \log L_x$, which is slightly steeper ($B = 0.32 \pm 0.01$) than indicated by observations ($B = 0.265 \pm 0.035$), but within observational errors. In contrast, the standard $\Omega = 1$ model predicted temperatures which were significantly too high. The mean luminosity-weighted temperature is 1.8 keV, dramatically lower (by a factor of 3.5) than that found in the $\Omega = 1$ model, and the evolution far slower (−30% vs. −50%) than in the $\Omega = 1$ model to redshift $z = 0.5$. A modest average temperature gradient in clusters is found with temperatures dropping to 90% of central values at 0.4 h^{-1} Mpc and to 60% of central values at 0.9 h^{-1} Mpc.

Examining the ratio of gas-to-total mass in the clusters, we find a slight antibias [$b = 0.9$ or $(\Omega_{gas}/\Omega_{tot})_{cl} = 0.083 \pm 0.007$], which is consistent with observations [$(\Omega_{gas}/\Omega_{tot})_{obs} = 0.097 \pm 0.019$ for the Coma cluster for the given value of h, cf., White 1991].

Subject headings: cosmology: theory — dark matter — galaxies: clustering — galaxies: evolution — hydrodynamics — methods: numerical — radiation mechanisms: nonthermal — X-rays: galaxies

1. INTRODUCTION

In the preceding two papers of this series (Kang et al. 1994, hereafter KCOR; Bryan et al. 1994), we have examined the properties of X-ray clusters in the standard *COBE*-normalized cold dark matter (CDM) universe and reached two primary conclusions: (1) the standard CDM model overproduces bright X-ray clusters ($L_x > 10^{43}$ ergs s^{-1}) by a factor in excess of 5; (2) observations of the ratio of gas-to-total mass in great clusters of galaxies, combined with our simulations, imply that we live in an open ($\Omega = 0.2$–0.3) universe (with or without a cosmological constant). There are other well-known difficulties with the standard CDM scenario (cf. Ostriker 1993 for a review), and there are advantages to open CDM models (cf. Efstathiou 1992) which arise from other considerations, independent of cluster X-ray properties. Motivated by this knowledge, we turn in this paper to examine a $\Omega < 1$ CDM model with a cosmological constant. We wish to investigate the difference in the evolutionary behavior as well as the $z = 0$ properties of X-ray clusters in these two different models. There is every expectation that cluster X-ray properties should provide a strong dis-

criminant among cosmic theories. We will, throughout this paper, make comparisons with KCOR wherever it is possible, since that calculation was made with identical physical assumptions and with identical numerical modeling techniques adopted.

In § 2 we outline the method and initial conditions, in § 3 we give the results, and in § 4 we assemble our conclusions.

2. METHOD AND INITIAL CONDITIONS

2.1. *Method*

The superiority of the new Total Variation Diminishing (TVD) code over conventional hydrodynamic codes (e.g., Cen 1992) and various tests of the code have been presented in Ryu et al. (1993); essentially the shock capturing technique improves resolution by approximately a factor of 2–3 for a given grid (i.e., nominal resolution).

The simulation reported on in this paper did not include any atomic processes, i.e., no cooling or heating was added, except for the adiabatic cooling due to the general expansion of the universe, and "heating" occurs only due to adiabatic compression or to entropy generation at shock fronts. For the hot gas, which we will discuss in this paper, this approximation is valid, since the cooling time exceeds the Hubble time by a fair margin. One can, after the fact, compute the emissivity with allowance for line emission. Doing this would increase the computed luminosity significantly at and below 1 keV but would have little effect in the 2–10 keV band. We will return to this important matter in a subsequent paper devoted to a comparison with observations. Here we wish, primarily, to contrast $\Omega < 1$, and standard $\Omega = 1$, variants of the CDM scenario.

2.2. *Initial Conditions*

We adopt a CDM + Λ model with the following parameters: $n = 1$, $h = 0.6$, $\Omega = 0.45$, $\Omega_b = 0.043$, $\lambda = 0.55$, and $\sigma_8 = 0.77$. Note that the amplitude normalization of the power spectrum is determined by *COBE* observations (Efstathiou, Bond, & White 1992; Kofman, Gnedin, & Bahcall 1993) parameterized by σ_8 to translate into conventional notation. This chosen value of σ_8 corresponds to a "bias" of $b \equiv 1/\sigma_8 = 1.30$, close to what is physically expected on this scale (cf. Cen & Ostriker 1992, 1993) lending further credibility to the adopted model. Our box size is 85 h^{-1} Mpc with $N = 270^3$ cells and 135^3 dark matter particles, so our nominal resolution is 0.31 h^{-1} Mpc with our real spatial resolution slightly worse than this. The box size is determined by a compromise between two considerations. A larger box would allow longer waves and give us more of the rare, high-temperature, high-luminosity clusters. A smaller box (with a fixed N) would allow us to resolve the cluster structure better. The choice of Ω_b is consistent with light element nucleosynthesis (Walker et al. 1991). The power spectrum transfer function is computed using the method described in Cen, Gnedin, & Ostriker (1993). Gaussian initial conditions are used and the same set of random numbers adopted as in KCOR.

3. RESULTS

The X-ray clusters in the simulation are identified as follows. We first calculate the total X-ray luminosity due to thermal bremsstrahlung (assuming primeval composition and neglecting lines) for each cell, given the cell density and temperature, assuming that hydrogen and helium are fully ionized (which is always true in the regions like great clusters of galaxies). The detailed formulae were presented in KCOR. Note that in the following discussion all units of length are given in co-moving, not metric, coordinates.

First we tag all cells having total X-ray luminosity higher than 10^{38} ergs s^{-1}. This emissivity corresponds to 3.2×10^{39} ergs s^{-1} h^3 Mpc^{-3}, which is 3.2 times the mean box emissivity at $z = 0$, and is 9.1 times the mean at $z = 3$. The number of X-ray bright cells defined in this way is 47,826, which comprises a fraction 2.4×10^{-3} of the box volume. These are selected as X-ray bright cells. Then we find the local maxima (by comparing $L_{\rm ff}$ of each X-ray bright cell with that of 26 neighboring cells) and identify them as the centers of the X-ray clusters. Having defined the centers of the X-ray clusters, we go back to the whole simulation box to define our X-ray clusters. We analyze the simulation in the following two different ways (which correspond to spheres of radius 0.5 h^{-1} Mpc and 1.0 h^{-1} Mpc). First, each cluster core consists of 27 cells (26 cells surrounding the central cell plus the central cell). These 27 cells are weighted so that the total volume of the cluster equals the volume of a sphere of radius 0.5 h^{-1} Mpc as appropriate for observationally defined X-ray clusters (see KCOR for details). A similar algorithm is used for the 1.0 h^{-1} Mpc volumes.

Our (85 h^{-1} Mpc)^3 box at $z = 0$ contained (0, 0) clusters with (total, core) luminosity brighter than 10^{45} ergs s^{-1}, (1, 0) brighter than 10^{44} ergs s^{-1}, (10, 5) brighter than 10^{43} ergs s^{-1}, (66, 40) brighter than 10^{42} ergs s^{-1}, and (257, 174) brighter than 10^{41} ergs s^{-1}. We explain the absence of clusters brighter than 10^{45} ergs s^{-1} simply due to the size of our box. An additional factor of at least 2 in scale (and 8 in computer resources) would be required to significantly improve on the quoted results. An immediate comparison to the KCOR results is possible if one notes that for $L_x > 10^{44}$ ergs s^{-1}, the KCOR paper found (8, 1) clusters with (total, core) luminosity, higher than the specified limit compared to (1,0) in this work. The difference is significant at this level of luminosity and we will see below (Figs. 1*b* and 4*b*) that, while the standard CDM model overproduces bright X-ray clusters, this model provides an adequate fit to observations. The fraction of the box in brightest cells which provide (50%, 90%) of the total box emissivity is (3.8×10^{-5}, 8.8×10^{-4}).

It is convenient to fit the luminosity function to the three-parameter Schechter function

$$n(L)dL = n_0(L/L^*)^{-\alpha}e^{-L/L^*}d(L/L^*) . \quad (1)$$

Luminosity functions for cluster cores were computed in four frequency bands: total (bolometric) luminosity, 0.3–3.5 keV, 0.5–4.5 keV, and 2–10 keV, and are displayed in Figures 1*a*, 2*a*, 3*a*, and 4*a*, respectively. The results for entire clusters (emission from a 1 h^{-1} Mpc sphere) are presented for the same frequency bands in Figures 1*b*, 2*b*, 3*b*, and 4*b*. The figures show the domain of cluster properties in which the observations and our computations overlap most: 10^{40} ergs s^{-1} $\le L_x \le 10^{44}$ ergs s^{-1} and $0 \le z \le 1$. Also shown in Figures 1*b* and 4*b* (shaded areas) are the observations from Henry & Arnaud (1991) and from Henry (1992), respectively. The comparison shown in Figure 4*b* is the more reliable one, since line processes (omitted in our computation) are unimportant in the 2–10 keV band.

We see that the computed number densities of bright clusters ($h^2L \ge 10^{43}$ ergs s^{-1}) are in accord with the observed ones, while in KCOR we found that those of the CDM model are above the observed mean by a factor of ~ 5. We have computed approximate Schechter function fits to the results, with the numerical parameters (n_0, L^*, α) as a function of redshift collected in Table 1, and the simulated data extended to $z = 5$.

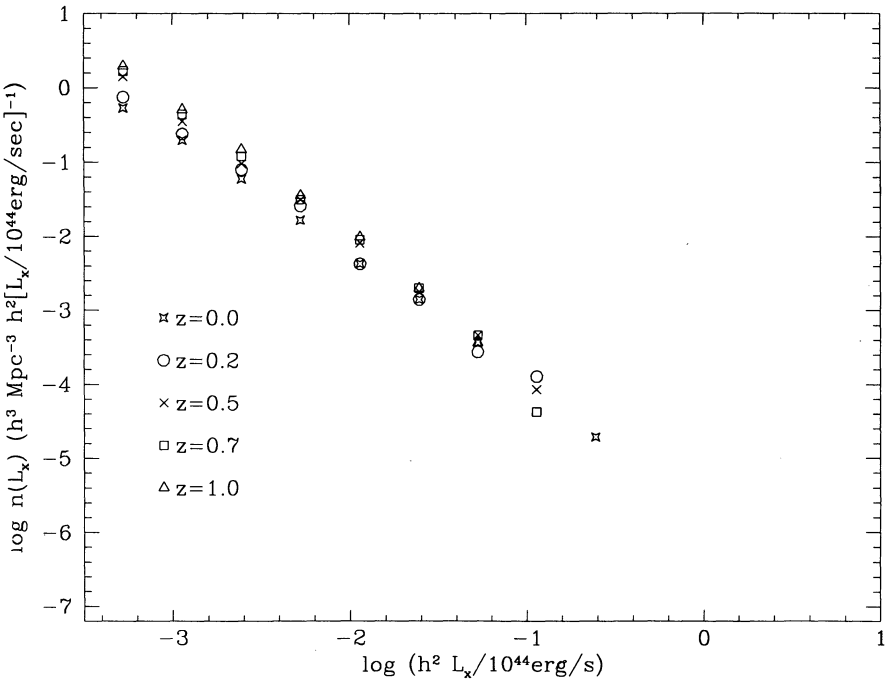

FIG. 1*a*

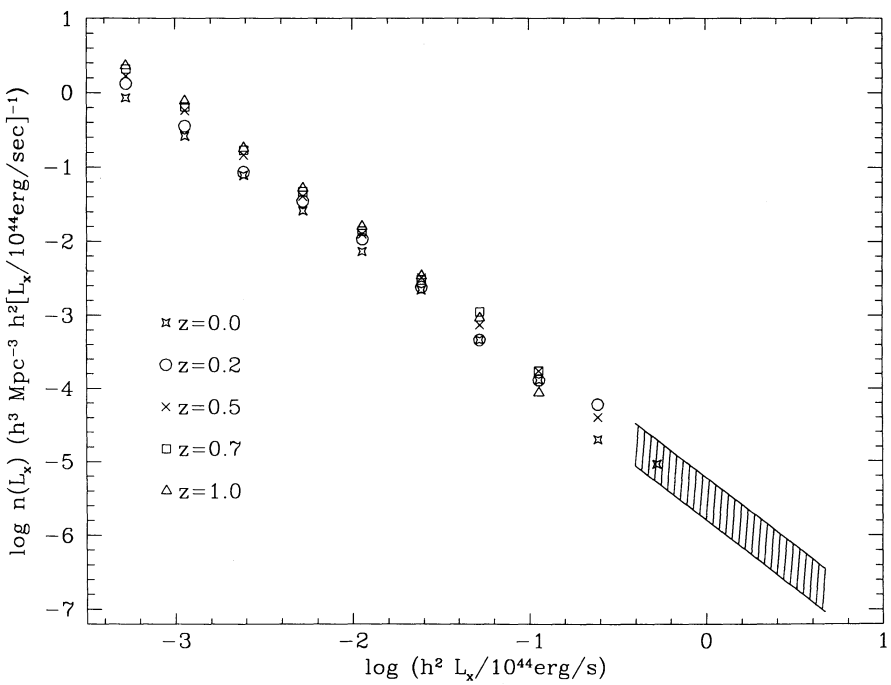

FIG. 1*b*

FIG. 1.—(*a*) The X-ray cluster bremsstrahlung luminosity (from central $<0.5\,h^{-1}$ Mpc regions) function integrated over the whole frequency range at five different redshifts z = (0, 0.2, 0.5, 0.7, 1.0). (*b*) The X-ray cluster bremsstrahlung luminosity (from $<1.0\,h^{-1}$ Mpc region) function integrated over the whole frequency range (*filled dots*) at the same five different redshifts. The *shaded area* shows the observations (Henry & Arnaud 1991; $\{3.1^{+4.5}_{-1.8} \times 10^{-6} h^3$ Mpc^{-3} $h^2[L_{44}(\mathrm{bol})]^{-1}\}$ $\times [h^2 L_{44}(\mathrm{bol})]^{-1.85\pm0.4}$).

Also in Table 1 we integrate over the cluster luminosity function, using the Schechter fit, $j_{\mathrm{cl}} \equiv n_0 L^*\Gamma(2-\alpha)$, showing the results in column (8). We give also, in column (9), the total emissivity from the box as j_{gas}, which includes the emission from lower density regions further from cluster cores than 1.0 h^{-1} Mpc and also from clusters whose central emissivity is less than our cutoff value. Note that L_x^* is in units of 10^{44} ergs s^{-1}; n_0, $n(L > 10^{43})$ and $n(L > 10^{44})$ are in units of $10^{-6}h^3$ Mpc^{-3}; j_{cl} and j_{gas} are in units of 10^{40} ergs s^{-1} h^{-3} Mpc^3, and j_{cl} may be larger than j_{gas} due to the inaccuracy of the Schechter fit.

We estimate that α is well constrained (± 0.03) and that the

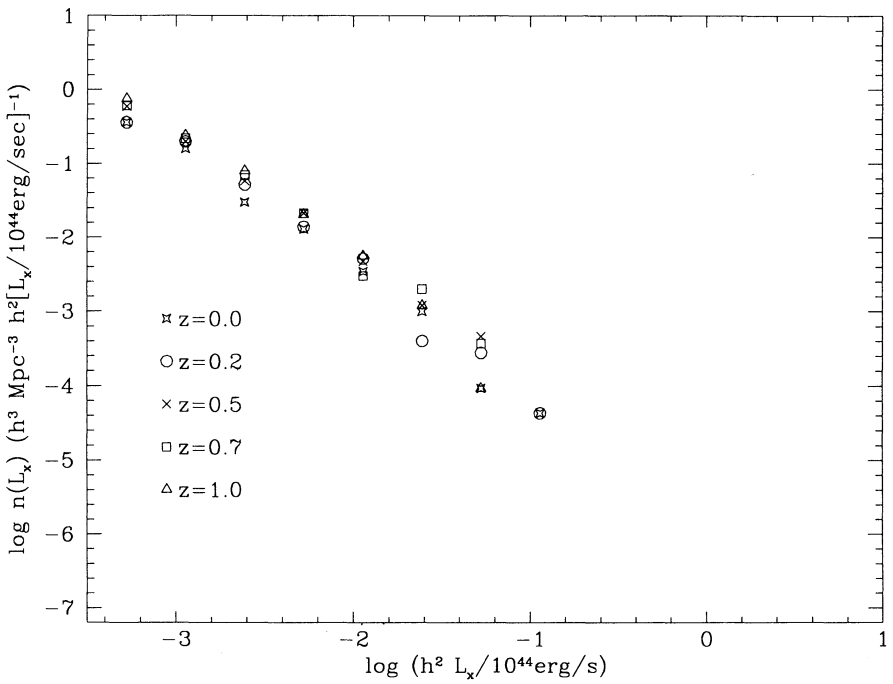

FIG. 2*a*

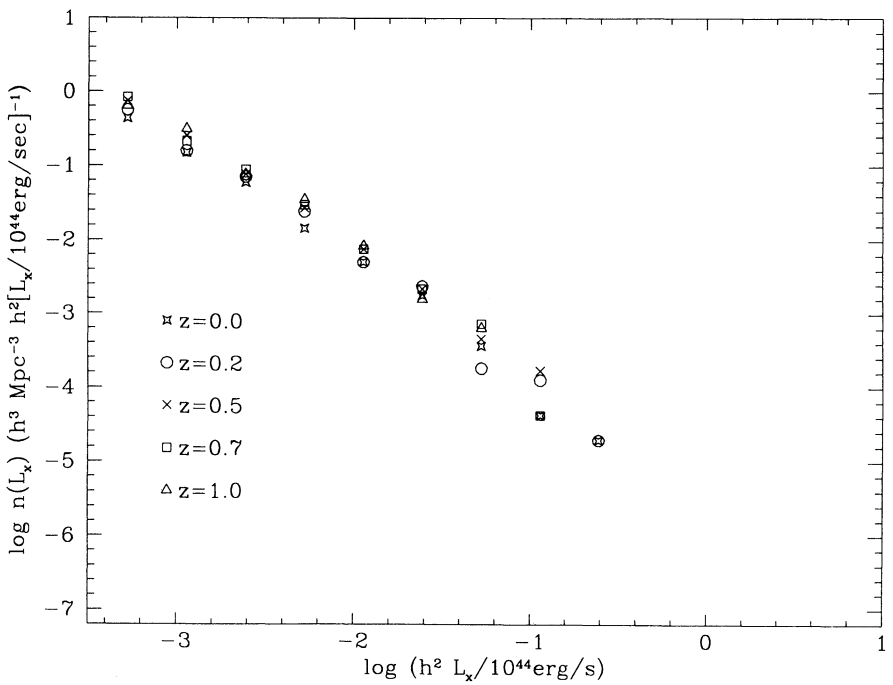

FIG. 2*b*

FIG. 2.—Same as Fig. 1 but for the luminosities integrated over 0.3–3.5 keV frequency bin

product n_0L^* is also fairly well constrained, but individual values (n_0, L^*) are poorly determined because L^* is dependent on the quite uncertain highest luminosity clusters. To estimate the purely statistical uncertainty, we reanalyzed the $z = 0$ data from the lower panel of Table 1A (total, integrated X-ray cluster properties) looking separately at two halves of the box. The fractional differences ($|\Delta Q/Q|$) for $Q \equiv (\alpha, L_x^*, kT_x, n_0, j_{cl}, j_{gas})$ were found to be (0.0062, 0.90, 0.62, 0.74, 1.31, 0.76) respectively. The fact that even the integral j varies significantly between the two halves of the box reminds us again of the "cosmic variance." Our sample volume is not large enough to give us a robust estimate for the cosmic mean value of j. Note that the variances of all the quantities (except for α) in this model are larger than those in the CDM model (KCOR), presumably due to the fact that this CDM + Λ model has relatively more large-scale power than the CDM model, indicating

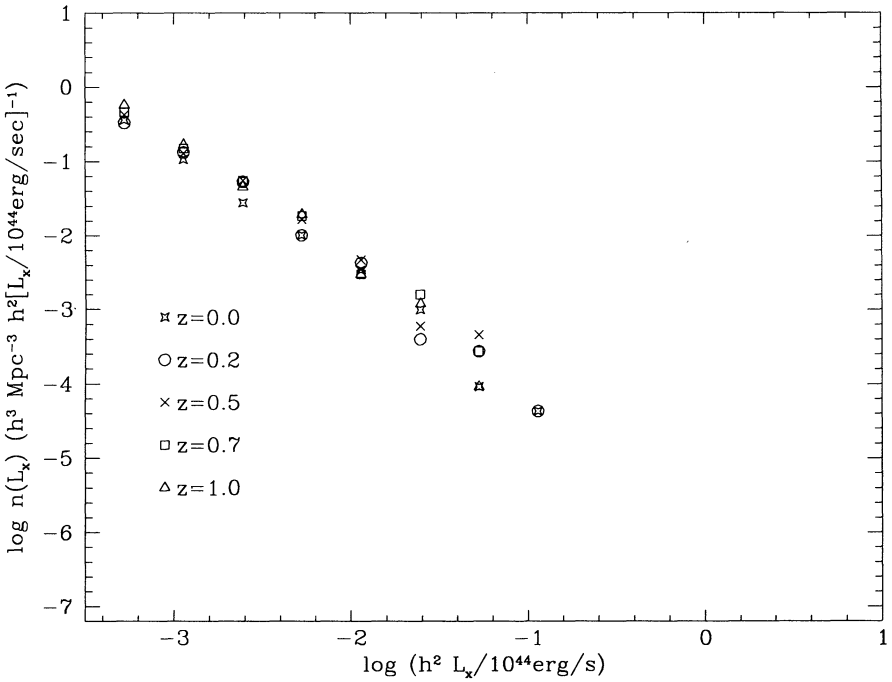

FIG. 3*a*

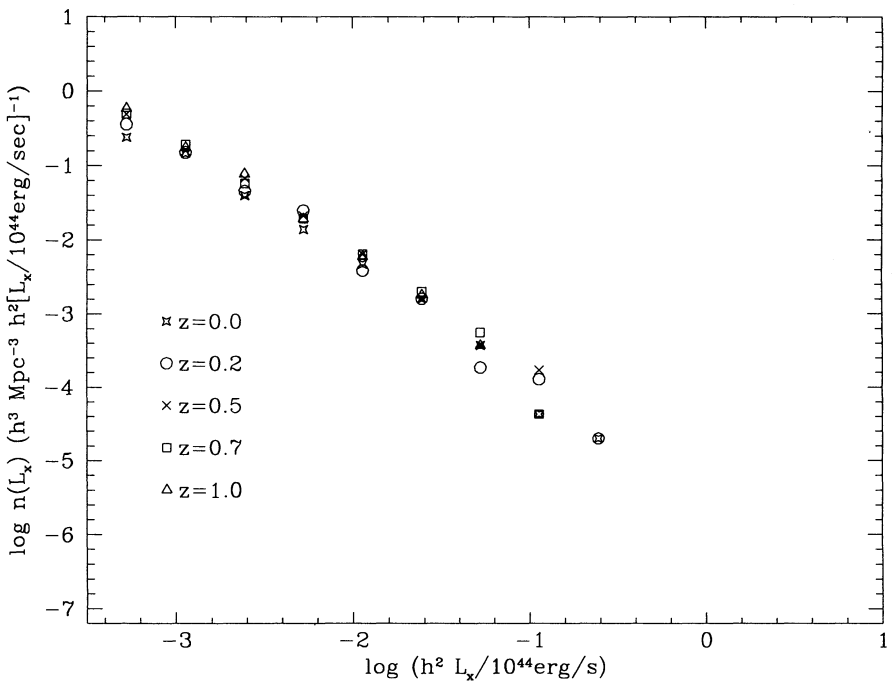

FIG. 3*b*

FIG. 3.—Same as Fig. 1 but for the luminosities integrated over 0.5–4.5 keV frequency bin

that a larger box is clearly desirable. This, of course, is related to the virtues of open models: they typically have relatively more large-scale power and thus match better a variety of large-scale structure observational constraints (cf., e.g., Efstathiou et al. 1993) than do $\Omega = 1$ models.

We see that the cluster cores, as we have defined them, contain between $\frac{1}{3}$ and $\frac{1}{2}$ of the total X-ray emission in the regions studied, comparable to the results of KCOR. The total cluster luminosity in the box is typically $\frac{3}{4}$ of the X-ray emission from the box, the same level was found in the CDM model (KCOR). This fraction depends on energy, as one can see by comparing Tables 1B and 1D. Since most of the very high temperature gas is in the central regions of clusters, the fraction of the total emission from identifiable clusters in the 2–10 keV region approaches unity. For the total luminosity the Schechter α parameter is ~ 1.55 (as compared to 1.50 in KCOR) with

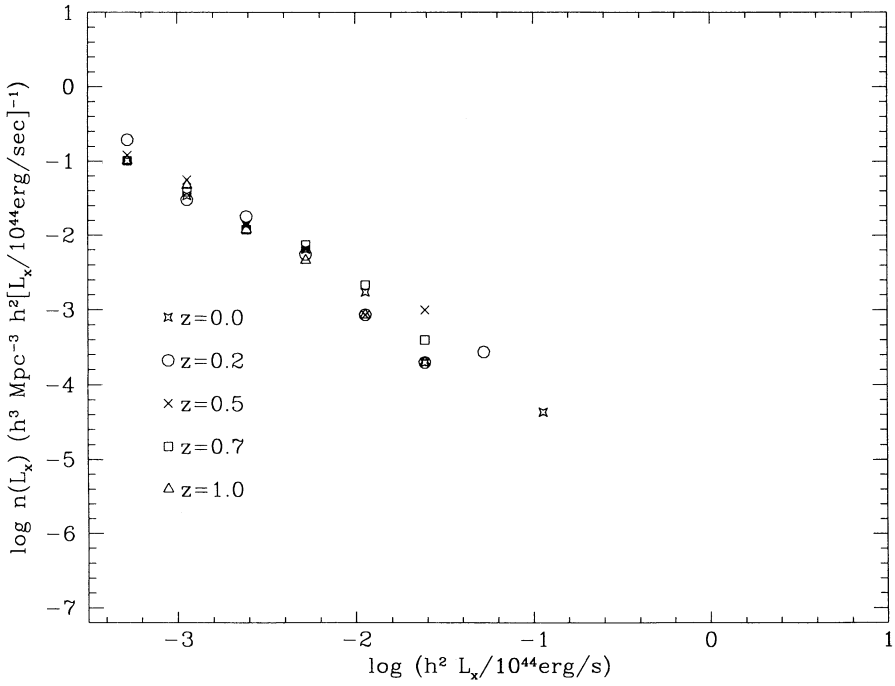

FIG. 4*a*

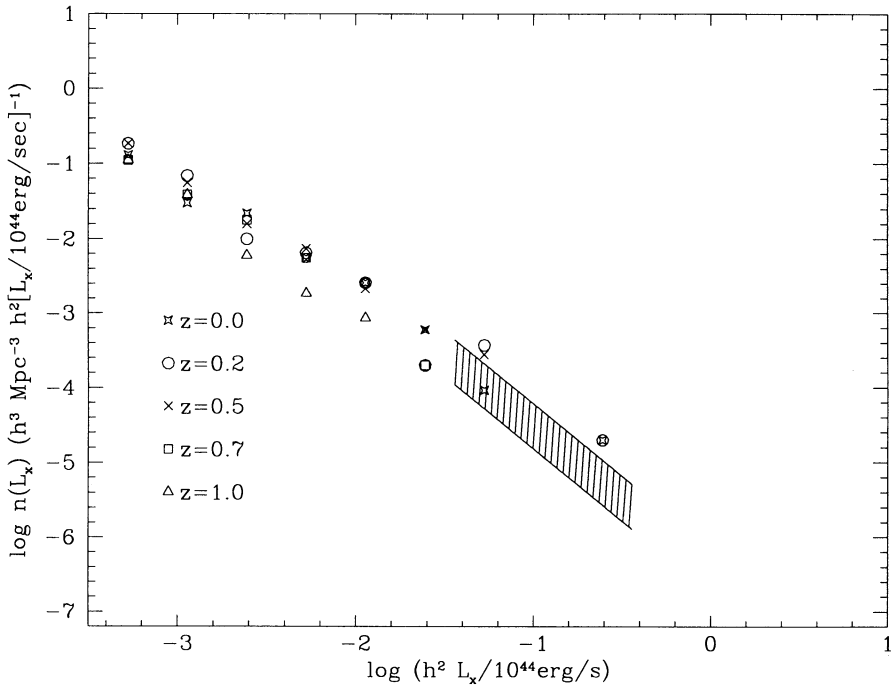

FIG. 4*b*

FIG. 4.—Same as Fig. 1 but for the luminosities integrated over 2–10 keV frequency bin. The shaded area in (*b*) indicates observations (Henry 1992).

little evolution, and α, for the few keV bands is typically slightly flatter at 1.4. For $\alpha < 2$, as we have noted, most of the luminosity arises from bright clusters. Observationally $\alpha = 1.9$–2.0; so this model provides a marginally better fit than does the standard $\Omega = 1$, CDM model. Allowance for line emission processes would increase the luminosity of the lower luminosity (low-temperature) clusters more than the high-luminosity (high-temperature) clusters, still further improving the fit. Without a careful treatment of line emission, it would be premature to say if the fit to the slope of the luminosity function, as represented by α in this model, is adequate.

The number density of bright clusters peaks at intermediate redshift, and the typical luminosity is (for small redshift) relatively constant, so there is a peak emissivity at $\sim z = 0.2$–0.5 for the several keV bands. Thus, crudely speaking, in this model one expects weak "positive" evolution until nearly

TABLE 1A

PARAMETERS OF SCHECHTER FITS FOR THE X-RAY CLUSTER LUMINOSITY FUNCTION INTEGRATED OVER THE ENTIRE FREQUENCY RANGER

z (1)	α (2)	$L_x^*(10^{44})$ (3)	$k\bar{T}_x$(keV) (4)	n_0 (5)	$n(L > 10^{43})$ (6)	$n(L > 10^{44})$ (7)	j_{cl} (8)	j_{gas} (9)
X-Ray Cluster Core Luminosity[a]								
0	1.52	0.54	1.79	4.52	3.9	7.4×10^{-2}	0.045	0.10
0.2	1.60	1.16	1.51	2.39	4.7	2.4×10^{-1}	0.061	0.12
0.5	1.55	0.27	1.05	10.7	4.2	1.1×10^{-2}	0.053	0.14
0.7	1.54	0.15	0.84	19.1	3.1	4.8×10^{-4}	0.055	0.13
1	1.53	0.11	0.64	27.7	2.6	4.1×10^{-5}	0.057	0.12
2	1.58	0.043	0.31	37.9	0.28	8.8×10^{-12}	0.034	0.077
3	1.93	0.22	0.14	1.14	0.38	2.1×10^{-4}	0.035	0.035
5	1.90	0.11	0.054	0.37	3.1×10^{-2}	2.3×10^{-7}	0.0039	0.0086
X-Ray Cluster Total Luminosity[b]								
0	1.56	1.74	1.55	2.56	6.6	0.54	0.090	0.10
0.2	1.56	1.86	1.29	3.14	8.5	0.73	0.12	0.12
0.5	1.54	0.59	0.91	9.64	9.2	0.20	0.11	0.14
0.7	1.50	0.29	0.72	20.4	8.6	3.2×10^{-2}	0.10	0.13
1	1.48	0.15	0.58	36.3	6.0	1.0×10^{-3}	0.093	0.12
2	1.59	0.082	30.4	0.30	1.5	1.1×10^{-6}	0.054	0.077
3	1.78	0.046	0.15	15.1	0.11	9.4×10^{-12}	0.029	0.035
5	1.90	0.020	0.020	3.56	3.7×10^{-4}	9.8×10^{-24}	0.0068	0.0086

NOTES.—Here L_x^* is in units of 10^{44} ergs s^{-1}; n_0, $n(L > 10^{43})$ and $n(L > 10^{44})$ are in units of $10^{-6}h^3$ Mpc^{-3}; j_{cl} and j_{gas} are in umits of 10^{40} ergs s^{-1} h^{-3} Mpc^3, and j_{cl} may be larger than j_{gas} due to the inaccuracy of the Schechter fit.

[a] $<0.5\,h^{-1}$ Mpc.

[b] $<1\,h^{-1}$ Mpc.

TABLE 1B

PARAMETERS OF SCHECHTER FITS FOR THE X-RAY CLUSTER LUMINOSITY FUNCTION IN 0.3–3.5 keV BAND

z (1)	α (2)	L_x^* (3)	n_0 (4)	$n(L > 10^{43})$ (5)	$n(L > 10^{44})$ (6)	j_{cl} (7)	j_{gas} (8)
X-Ray Cluster Core Luminosity[a]							
0	1.45	0.22	5.86	1.7	2.4×10^{-3}	0.021	0.060
0.2	1.48	0.25	6.05	2.1	4.7×10^{-3}	0.026	0.070
0.5	1.45	0.26	9.32	2.4	9.3×10^{-3}	0.039	0.075
0.7	1.46	0.24	9.66	3.2	6.3×10^{-3}	0.038	0.069
1	1.35	0.22	8.40	2.4	4.0×10^{-3}	0.026	0.059
2	1.38	0.14	5.25	0.78	1.0×10^{-4}	0.011	0.020
3	1.60	0.13	3.02	0.38	1.9×10^{-5}	0.0087	0.0034
5	1.90	0.010	0.03	6.4×10^{-9}	4.4×10^{-26}	2.8×10^{-5}	2.6×10^{-5}
X-Ray Cluster Total Luminosity[b]							
0	1.42	0.44	6.37	4.1	6.0×10^{-2}	0.043	0.060
0.2	1.43	0.48	6.94	4.9	8.5×10^{-2}	0.052	0.070
0.5	1.37	0.32	14.2	6.3	4.2×10^{-2}	0.065	0.075
0.7	1.31	0.13	30.5	4.1	3.7×10^{-4}	0.052	0.069
1	1.36	0.16	22.4	4.2	1.3×10^{-3}	0.050	0.059
2	1.24	0.13	9.59	1.3	1.3×10^{-4}	0.015	0.020
3	1.60	0.35	0.77	2.5×10^{-3}	6.0×10^{-16}	0.0060	0.0034
5	1.90	0.01	0.050	1.1×10^{8}	7.4×10^{-26}	4.8×10^{-5}	2.6×10^{-5}

a $<0.5\,h^{-1}$ Mpc.

[b] $<1\,h^{-1}$ Mpc.

$z = 0.5$ and then negative evolution thereafter. The peak occurs at significantly lower redshift in the open model than in the standard CDM model. Figure 5*a* shows the comparison between the two models for the number density (per unit comoving volume) of clusters with rest frame luminosity greater than 10^{43} ergs s^{-1}. Figure 5*b* shows the number density (per unit comoving volume) of clusters with rest frame luminosity (integrated over the entire frequency range) greater than 10^{43} ergs s^{-1} for five different models. We see that it is the overall normalization on the relevant scale (σ_8) rather than Ω which is the dominant factor on the evolutionary behavior of the bright cluster number density. Physically, the rapid evolution occurs at an epoch when most of the bright clusters are collapsing. After that, the evolution still goes on due to processes such as merging, but it is relatively mild. Comparing the *COBE*-normalized standard CDM and the *COBE*-normalized

TABLE 1C

PARAMETERS OF SCHECHTER FITS FOR THE CLUSTER LUMINOSITY FUNCTION IN 0.5–4.5 keV BAND

z (1)	α (2)	L_x^* (3)	n_0 (4)	$n(L > 10^{43})$ (5)	$n(L > 10^{44})$ (6)	j_{cl} (7)	j_{gas} (8)
X-Ray Cluster Core Luminosity[a]							
0	1.39	0.21	6.32	1.7	2.2×10^{-3}	0.019	0.053
0.2	1.44	0.26	5.74	2.1	5.8×10^{-3}	0.024	0.059
0.5	1.46	0.57	4.65	4.0	9.4×10^{-2}	0.044	0.061
0.7	1.39	0.16	12.1	2.2	6.7×10^{-4}	0.028	0.053
1	1.34	0.13	10.9	1.4	1.2×10^{-4}	0.019	0.042
2	1.33	0.054	9.30	0.18	7.2×10^{-10}	0.0068	0.012
3	1.58	0.025	5.2	3.5×10^{-3}	2.9×10^{-20}	2.7×10^{-4}	1.5×10^{-3}
5	1.65	0.09	1.60	9.2×10^{-2}	1.7×10^{-7}	0.004	5.4×10^{-6}
X-Ray Cluster Total Luminosity[b]							
0	1.36	0.44	6.46	4.0	6.4×10^{-2}	0.040	0.053
0.2	1.42	0.58	5.23	4.4	0.11	0.047	0.059
0.5	1.40	0.52	7.92	5.9	0.13	0.061	0.061
0.7	1.32	0.14	20.6	3.1	4.6×10^{-4}	0.038	0.053
1	1.31	0.12	22.4	2.6	1.3×10^{-4}	0.035	0.042
2	1.38	0.051	11.7	0.18	2.4×10^{-10}	0.0086	0.012
3	1.58	0.035	5.2	1.7×10^{-2}	4.3×10^{-15}	3.8×10^{-3}	1.5×10^{-3}
5	1.43	5.95	0.47	3.1×10^{-2}	8.8×10^{-8}	0.044	5.4×10^{-6}

[a] $<0.5\,h^{-1}$ Mpc.
[b] $<1\,h^{-1}$ Mpc.

TABLE 1D

PARAMETERS OF SCHECHTER FITS FOR THE X-RAY CLUSTER LUMINOSITY FUNCTION IN 2–10 keV BAND

z (1)	α (2)	L_x^* (3)	n_0 (4)	$n(L > 10^{43})$ (5)	$n(L > 10^{44})$ (6)	j_{cl} (7)	j_{gas} (8)
X-Ray Cluster Core Luminosity[a]							
0	1.22	0.088	9.84	0.67	2.4×10^{-6}	0.011	0.026
0.2	1.37	0.16	5.01	0.92	2.9×10^{-4}	0.011	0.024
0.5	1.34	0.15	6.70	1.1	2.5×10^{-4}	0.014	0.019
0.7	1.35	0.17	3.13	0.63	2.9×10^{-4}	0.0074	0.013
1	1.20	0.10	3.88	0.34	4.4×10^{-6}	0.0045	0.0078
2	1.17	0.081	0.79	4.7×10^{-2}	7.4×10^{-8}	7.0×10^{-4}	7.8×10^{-4}
3	1.13	0.018	0.14	2.9×10^{-5}	5.1×10^{-23}	2.8×10^{-5}	3.1×10^{-5}
5	1.80	0.004	0.01	1.8×10^{-16}	1.3×10^{-26}	1.8×10^{-6}	2.5×10^{-10}
X-Ray Cluster Total Luminosity[b]							
0	1.19	0.18	9.40	2.0	1.7×10^{-3}	0.020	0.026
0.2	1.35	0.30	5.88	2.4	1.3×10^{-2}	0.024	0.024
0.5	1.31	0.25	5.01	1.7	5.1×10^{-3}	0.016	0.019
0.7	1.32	0.20	2.82	0.71	8.1×10^{-4}	0.010	0.013
1	1.13	0.17	3.14	0.63	4.4×10^{-4}	0.0058	0.0078
2	1.10	0.10	1.25	0.11	1.8×10^{-6}	1.3×10^{-3}	7.8×10^{-4}
3	1.03	0.036	0.14	1.0×10^{-3}	1.7×10^{-15}	5.2×10^{-5}	3.1×10^{-5}
5	1.80	0.005	0.01	3.8×10^{-14}	1.5×10^{-26}	2.3×10^{-6}	2.5×10^{-10}

[a] $<0.5\,h^{-1}$ Mpc.
[b] $<1\,h^{-1}$ Mpc.

CDM + Λ models, negative evolution begins earlier and is stronger for the $\Omega < 1$ model. Allowance for cosmological effects would make both models evolve more negatively, but these effects would be exaggerated in the CDM + A case due to the rapid increase in luminosity distance (with redshift) in cosmologies with a significant cosmological constant. The different evolutionary path of the cluster luminosity function is the most significant difference we have found between $\Omega < 1$ and $\Omega = 1$ models. For example, Figure 5*b* shows more than an order of magnitude decline in the number density of clusters with 0.5–4.5 keV luminosity greater than 10^{43} ergs s^{-1} between redshift zero and two for the $\Omega < 1$ model, but it shows a slight increase for the standard CDM $\Omega = 1$ model.

We believe that the peak in emission seen at moderate redshift is real. The reasons for this are discussed in KCOR. The approximate Press-Schechter formalism, which does not allow for a variety of effects, cannot easily mimic the full nonequilibrium hydrodynamic treatment.

While the integrated X-ray emissivity evolves fairly slowly over the period surveyed in Table 1A, with a flat maximum

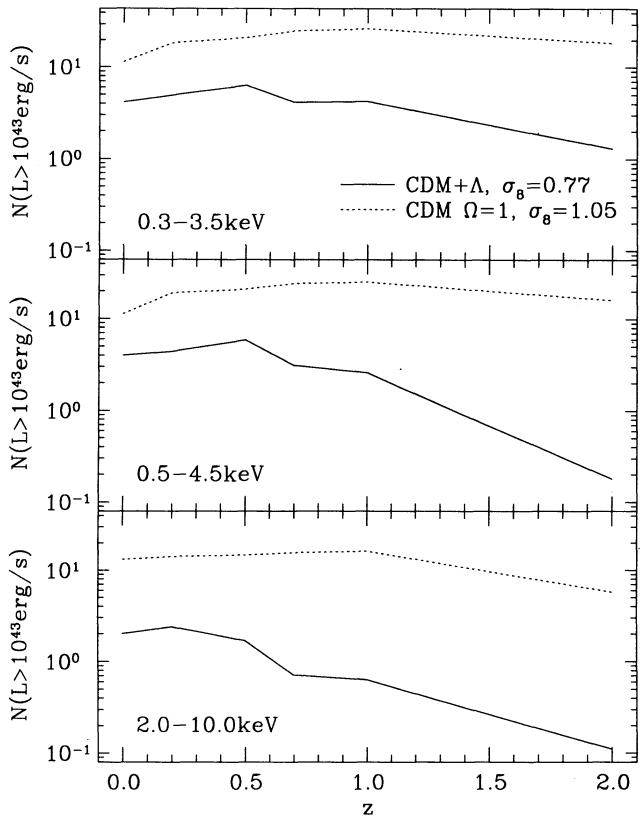

FIG. 5*a*

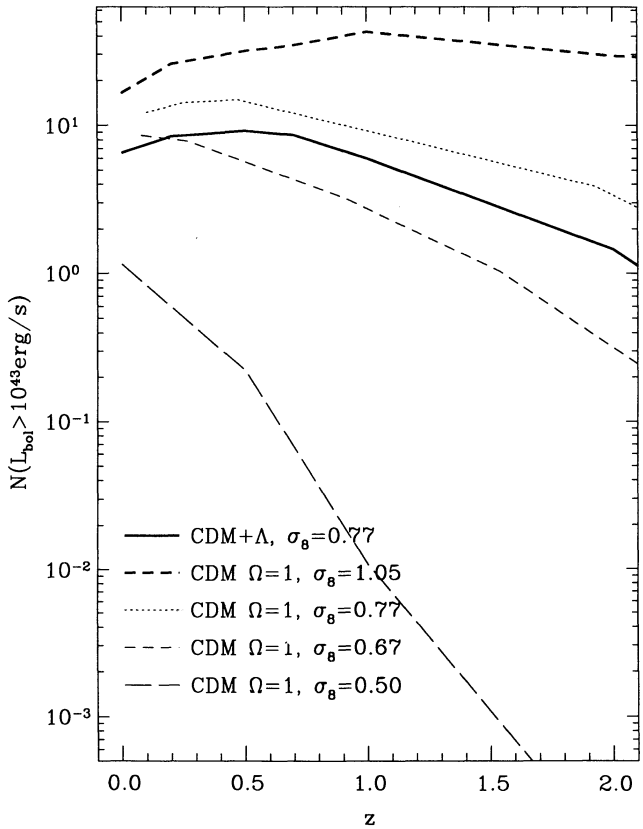

FIG. 5*b*

FIG. 5.—(*a*) Comparison between the two models for the number density (per unit comoving volume) of clusters with rest frame luminosity $> 10^{43}$ ergs s^{-1} for three X-ray bands. (*b*) The number density (per unit comoving volume) of clusters with rest frame luminosity (integrated over the entire frequency range) $> 10^{43}$ ergs s^{-1} for five different models.

between $z = 0.2$ and $z = 0.3$, L^* and n_0 tend to evolve more rapidly and in opposite directions. The primary difference which we find between this model and the CDM model (KCOR) is the evolution of the bright end X-ray clusters. In the $\Omega = 1$ CDM model (KCOR) we find that L^* is a monotonic decreasing function of redshift, while in this model we find L^* peaks at $z \sim 0.3$. The reason for this difference is the dramatically different behaviors of the universal expansion at later times in the two models. We expect that in a lower Ω model, L^* will clearly peak at an even higher redshift. The evolution of L^* should be observable and provide a powerful discriminant among cosmic models.

To highlight the negative evolution of the bright end of the luminosity function, we listed in the columns (5) and (6) of Table 1B–1D (cols. [6] and [7] of Table 1A) the comoving density of clusters having luminosity greater than 10^{43} ergs s^{-1} and 10^{44} ergs s^{-1}. For reasons stated earlier (based on our limited box size), we use the Schechter fit rather than direct counts to compute these columns. Comparing columns (4) and (6) ([5] and [7] of Table 1A), we see that, although the total number density n_0 of clusters increases with redshift (until $z \approx$ 1–2), the number density of the highest luminosity ($L_x > 10^{44}$ ergs s^{-1}) clusters decreases for $z > 0.5$. This is presumably one of the effects leading to the observational appearance of "negative evolution." Statistical fluctuations in our results are still quite significant due to the limited box size, especially for $n(L_x > 10^{44}$ ergs s^{-1}).

Redshift effects strongly exaggerate this tendency to observe negative evolution, since higher redshift clusters tended to have lower temperatures (cf. col. [4] of Table 1A and Fig. 6, and Fig. 13 below), and both effects will reduce the energy observed by satellites measuring the X-ray flux in high-energy bands. Note that the negative evolution in the density of clusters with $L > 10^{44}$ ergs s^{-1} more and more steep in Tables (1A → 1D) as one looks at higher energy bands, although statistical fluctuations are large.

The emission-weighted temperature, T_x, of each cluster is calculated and the distributions are shown in Figure 6. The arrow in each panel indicates the average cluster temperature (weighted by luminosity) at the given epoch. Also shown in Figure 6*b* is the observed temperature function from Henry & Arnaud (1991) as the cross-shaded area. Note that the computed temperature function is somewhat lower than the observed one, but we think that the limited size of our simulation box caused an omission from the computation of the highest temperature clusters; a bigger box is needed before we can have definite conclusions on this. We see that at all epochs the coolest clusters dominate the statistics (the turnover at low T_x is presumably caused by our definition of minimum cell luminosity to constitute an X-ray bright cell), but the mean is determined by the high-mass, high-luminosity, high-temperature end of the distribution. The mean temperatures, indicated by arrows, are included in column (3) of Table (1A). We will return to the issue of temperature evolution later.

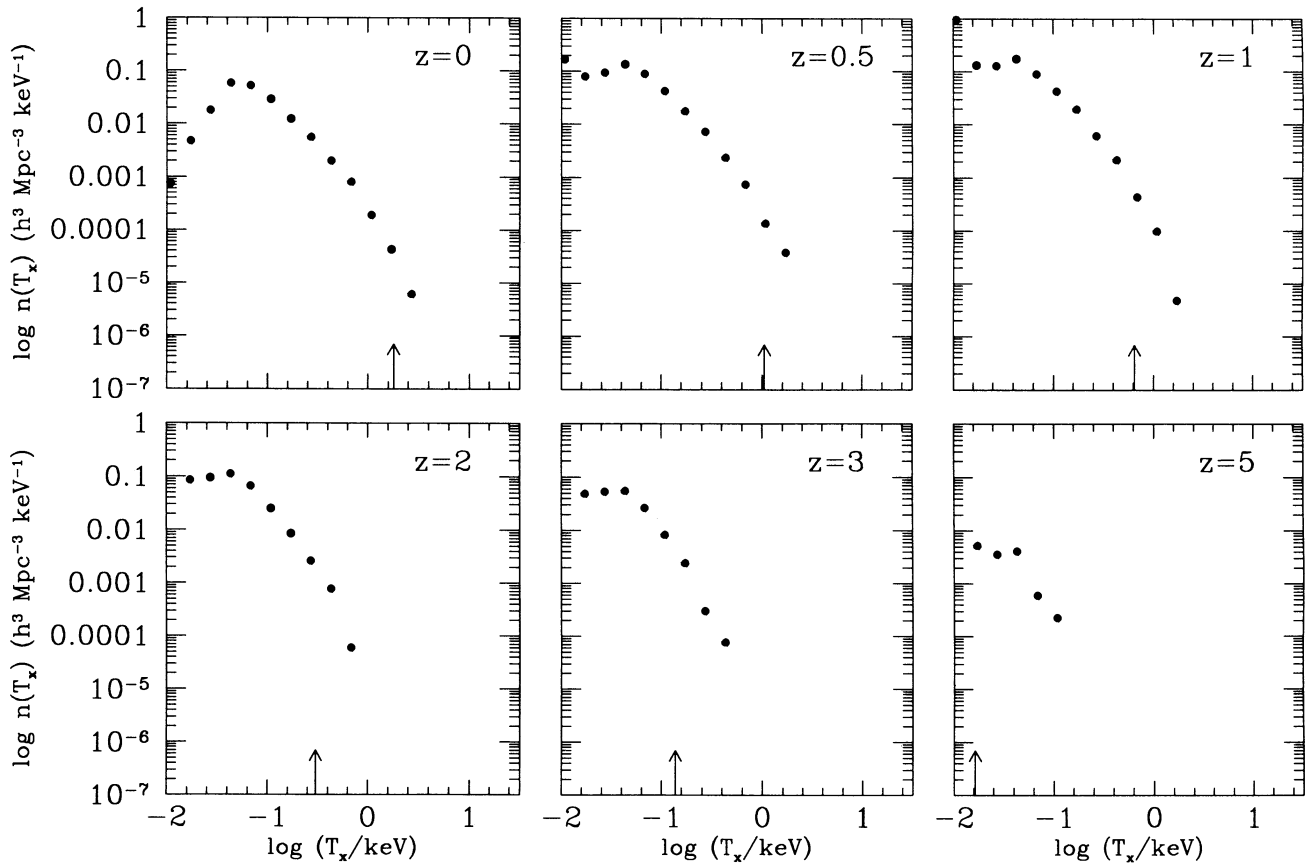

FIG. 6a

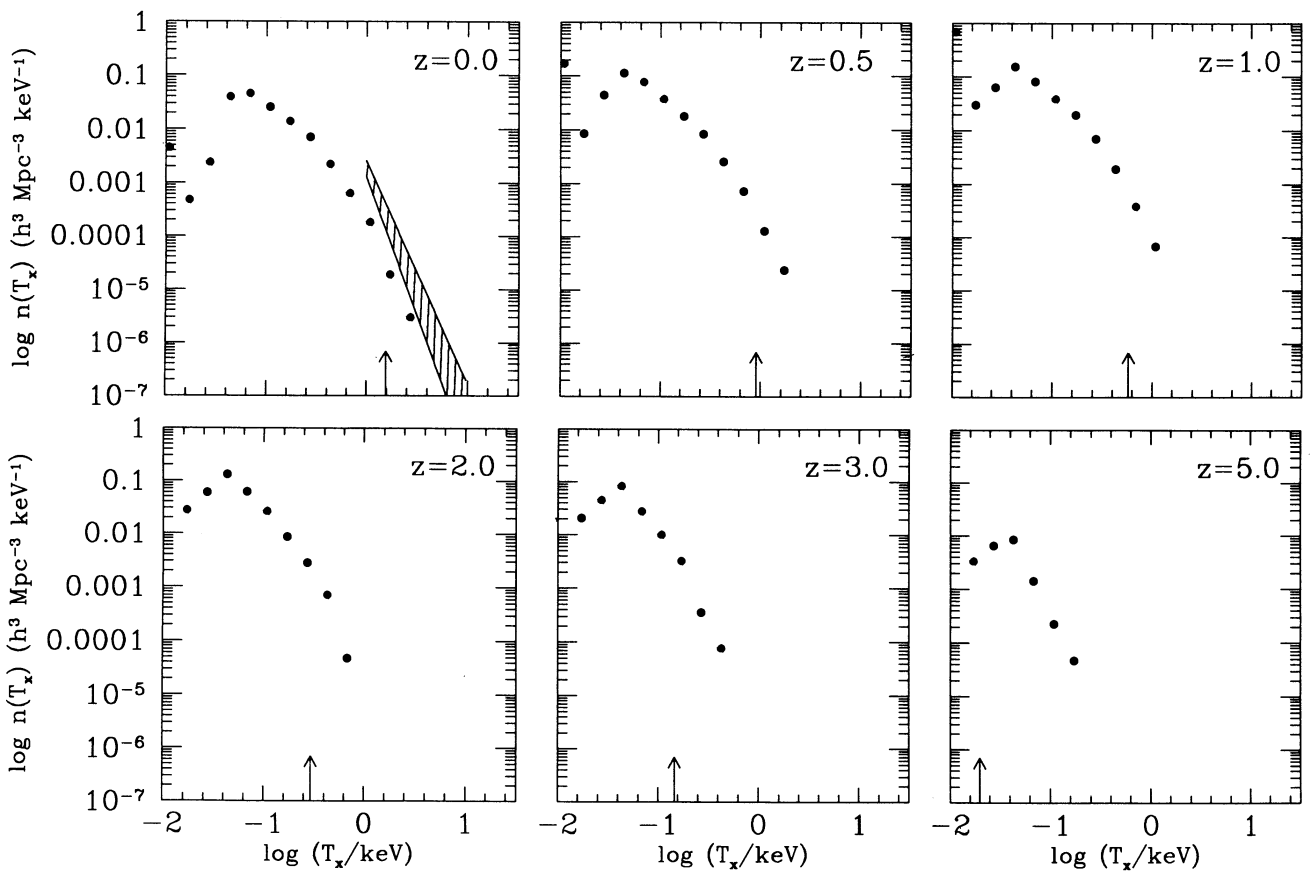

FIG. 6b

FIG. 6.—(*a*) The X-ray cluster temperature (T_x, emission-weighted temperature) function at six different redshifts $z = (0, 0.5, 1, 2, 3, 5)$. Arrows indicate the luminosity-weighted average temperature $\bar{T}_x$ at each epoch. In the first ($z = 0$) panel in (*b*) the *shaded area* is the observed temperature function from Henry & Arnaud (1991) $[(1.8^{+0.8}_{-0.5} \times 10^{-3} h^3\,\mathrm{Mpc}^{-3}\,\mathrm{keV}^{-1})(kT)^{-4.7\pm0.5}]$.

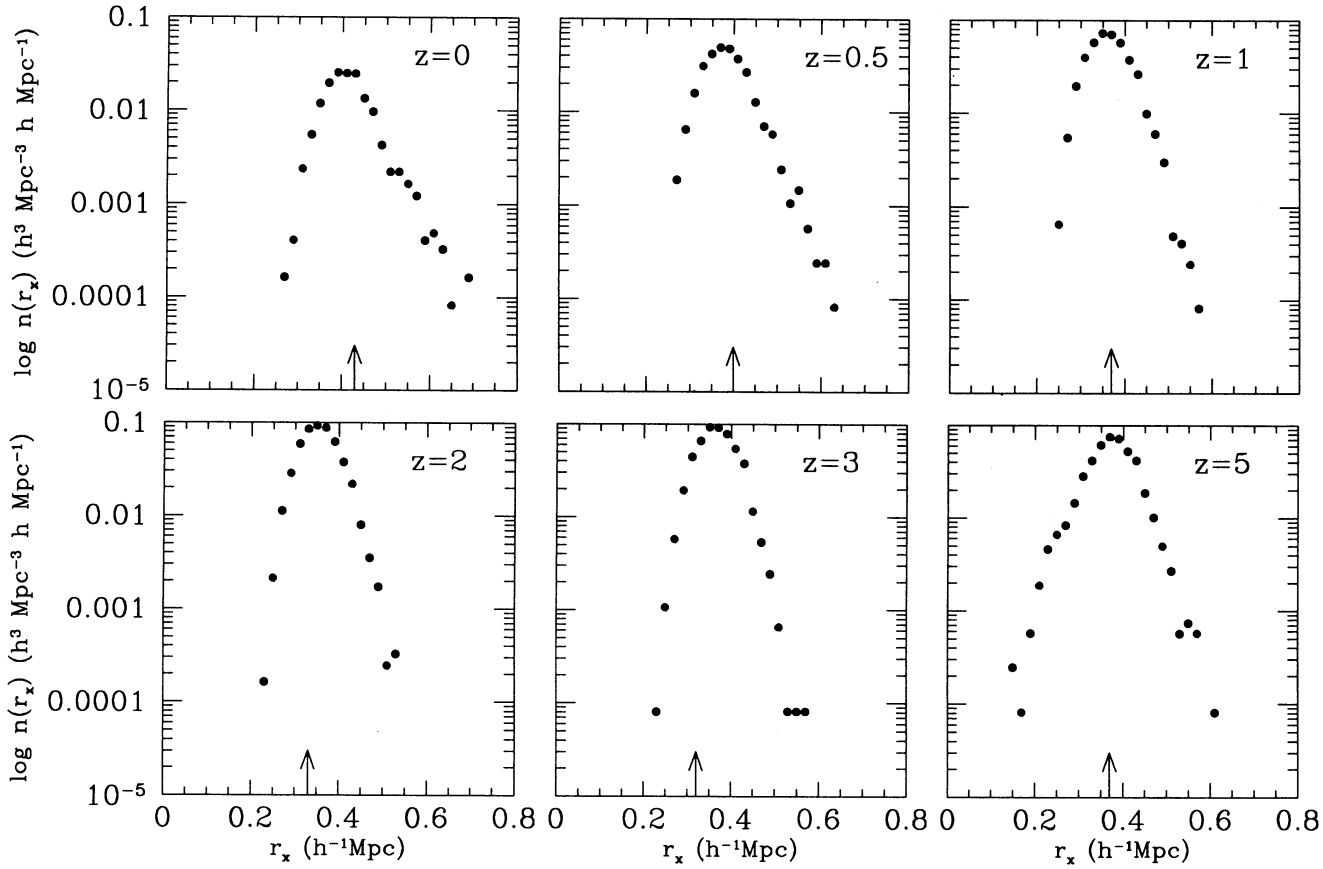

FIG. 7*a*

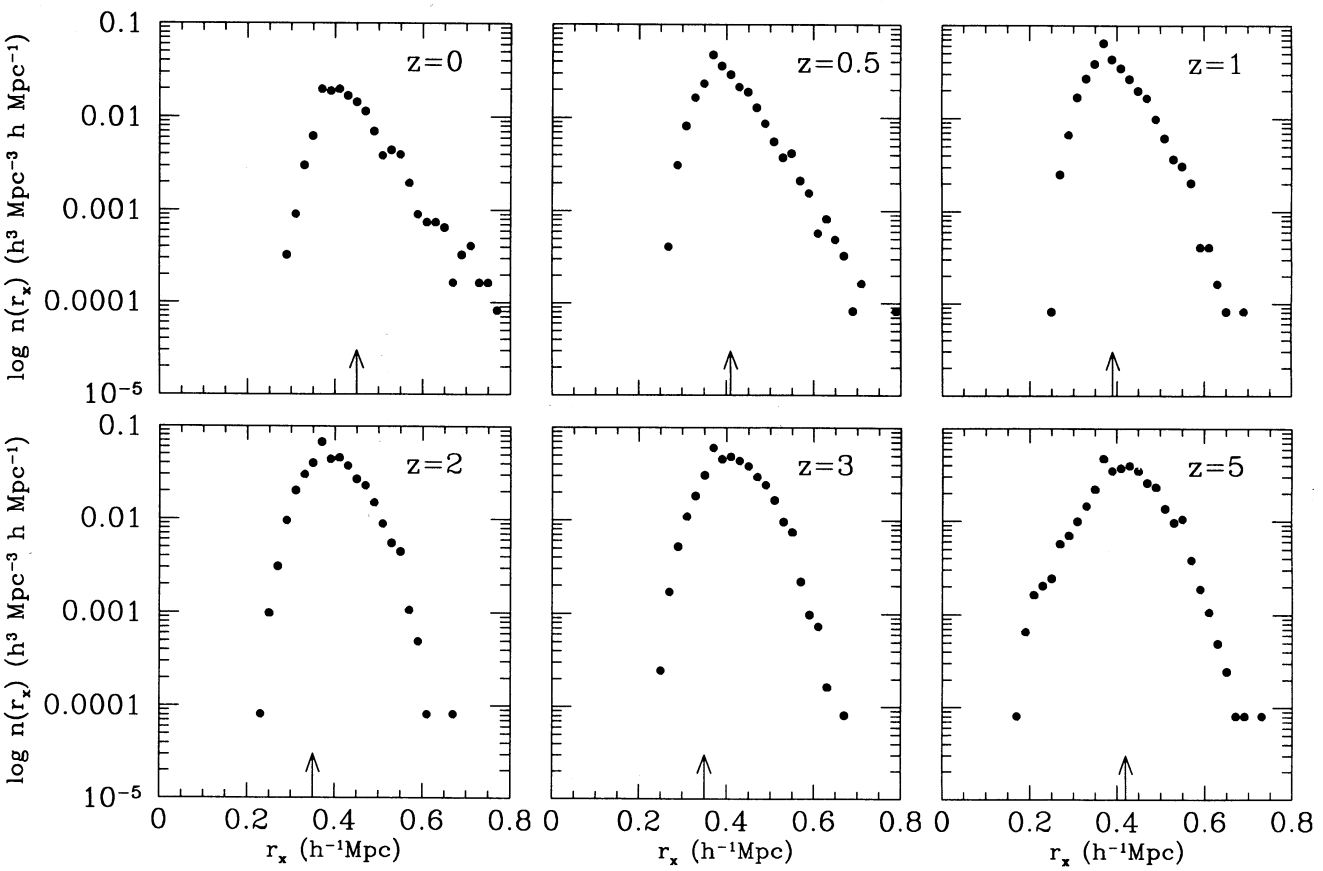

FIG. 7*b*

FIG. 7.—The X-ray cluster effective radius (r_x) distribution (cf. eq. [2]). Arrows indicate the luminosity-weighted effective radius at each epoch.

Looking ahead to Figure 8*a* below, we see the strong correlation found between T_x and total luminosity (clusters are shown at $z = 0$).

Now let us turn again to the total cluster luminosity (vs. core luminosity) as shown in the lower panels of the tables and in Figures 1*b*–4*b*, the quantity normally measured by satellite observations. The ratio of $(j_{\rm cl,tot}/j_{\rm cl,core})$ is near 2.0 ± 0.1 for the redshift range $0 < z < 1$; a similar value was found in KCOR.

We can also roughly estimate the effective radii of the clusters by assuming that the emission has a profile

$$j = \frac{j_0}{[1 + (r/r_x)^2]^2} \qquad (2)$$

and determining, from the ratio of the luminosity (integrated over frequency) of the central cell to the total cluster luminosity, the value of r_x which would produce this ratio. We show in Figure 7 the radii determined in this fashion. The peaks seen in the panels of Figure 7 are, of course, artificially induced by our cell size of $0.31\ h^{-1}$ Mpc, but the distribution to larger radii should be reasonably accurate. Arrows indicate the luminosity-weighted average values. Since brighter clusters tend to be resolved, these numbers should be reliable, but the arrows are uncomfortably close to the peaks of the curves, indicating that the most luminous clusters may be somewhat unresolved. We see a weak trend of increasing size with increasing time, which is in the theoretically anticipated direction. Longer wavelengths became nonlinear later, producing larger clusters, and smaller clusters merge to produce larger clusters with increasing time.

Now in Figures 8*a*–8*b* we show the scatter plots of (T_X, r_x) vs. L_x (bolometric). We see that there is a clear correlation between L_x and T_x. But we do not see any strong correlation between L_x and r_x. The best-fit lines (*dashed lines*) indicate a slope of $(0.36 \pm 0.01,\ 0.32 \pm 0.01)$ for (core, total) cluster region. In KCOR we found $(0.394 \pm 0.001,\ 0.375 \pm 0.001)$ for the CDM model. The observed correlation (cf. Fig. 8*a* shown as cross-shaded area) between $\bar{T}_x$ and total cluster luminosity is $\log_{10} \bar{T}_x(\mathrm{keV}) = \log_{10}(4.2^{+1.0}_{-0.8}) + (0.265 \pm 0.035) \log_{10}(h^2 L_{44})$, according to Henry & Arnaud (1991). In the region where a comparison can be made, the agreement with observations is good.

Next, we address temperature variations within clusters. Given our limited resolution, there is little that can be accurately determined on this issue from our simulations, but we are able to compare the central cell (volume $= 3.1 \times 10^{-2}\ h^{-1}$ Mpc^3) with the surrounding cells ($3^3 - 1^3$) (volume of size $5.9 \times 10^{-1}\ h^{-3}$ Mpc^3) and the cells surrounding these cells ($5^3 - 3^3$, vol $= 3.0\ h^{-3}$ Mpc^3). We define the ratio of the inner cell to the next shell as $T_c/T_{\rm shell}$ (volume-weighted average) and show the scatter diagram in Figure 9. No trend is seen with luminosity, and the median value, indicated by the dashed line, is 1.4. The cluster gas deviates significantly from isothermality, with a 5%–10% temperature decline typically found by a radius of 0.4–0.5 h^{-1} Mpc but a sharp fall-off is indicated for radii 1 h^{-1} Mpc. In Figure 10 we compare the (luminosity-

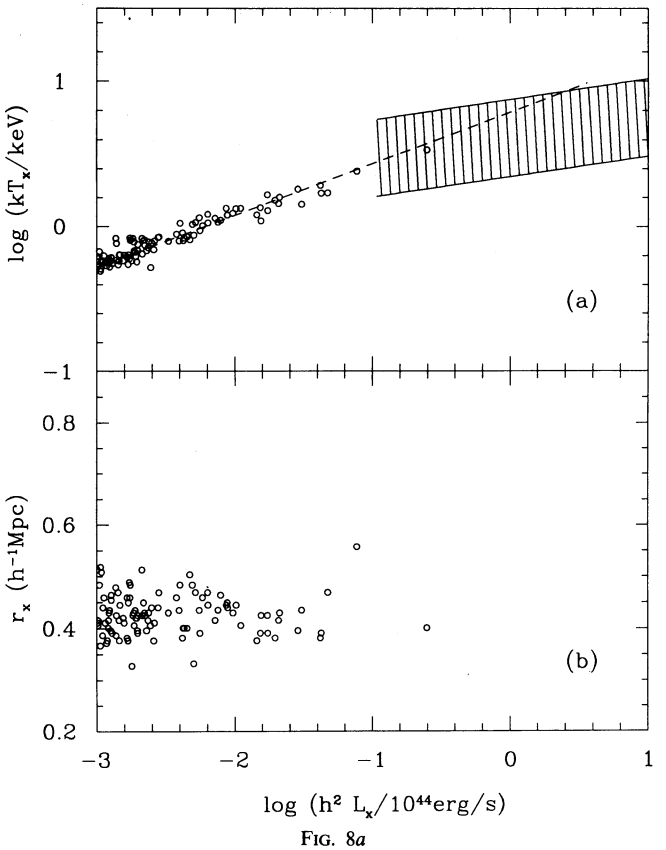

FIG. 8*a*

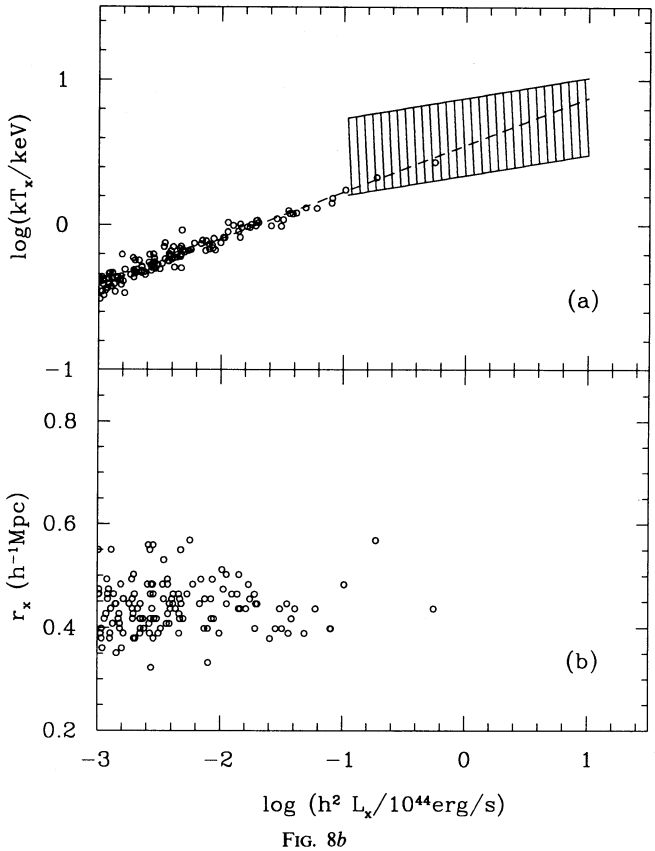

FIG. 8*b*

FIG. 8.—(*a*) The scatter plot of T_x vs. L_x at $z = 0$. *Shaded area* indicates the observations of Henry & Arnaud (1991). *Dashed line* is the best fit of the simulation results. Scatter plot of r_x vs. L_x at $z = 0$.

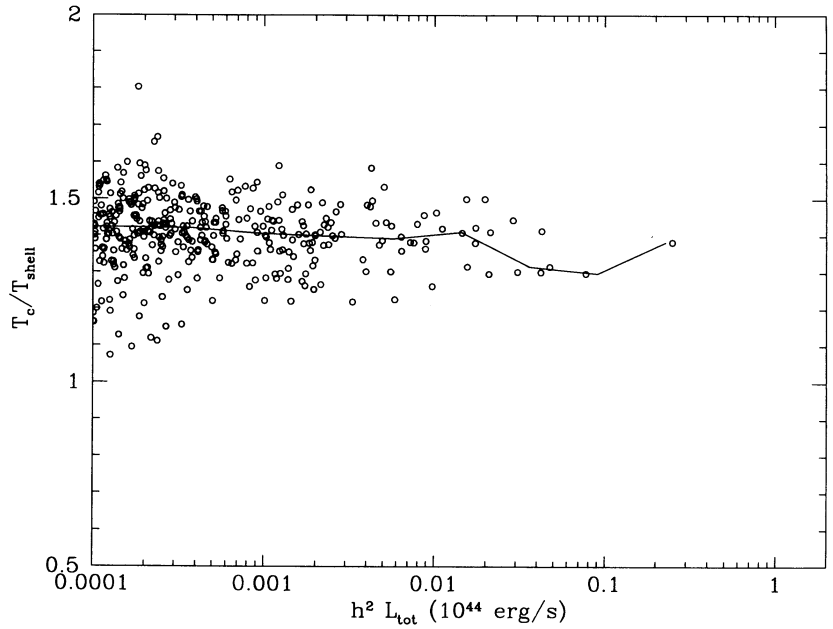

FIG. 9.—The ratio of the central cell temperature to the temperature of its surrounding shell (roughly one cell thick) as a function of L_{tot}.

weighted) temperatures found in the three regions noted above, normalized to the temperature in the central cell. The large dispersion is indicated by the error bar. Figures 9 and 10 show no significant differences from the analogous figures in the $\Omega = 1$ case (KCOR).

We show in Figures 11 and 12 the evolution of cluster core radius (in metric, not comoving, units) and temperature (both luminosity-weighted) as open circles. Solid dots are from the KCOR, $\Omega = 1$ computation. Also shown are the fits analytically predicted by Kaiser (1986) $R_x \propto (1 + z)^{-2}$ and $T_x \propto (1 + z)^{-1}$ for $\Omega = 1$, CDM model (*solid line*) from KCOR and this CDM + Λ model (*dotted line*) (note that Kaiser's prediction is valid for $\Omega = 1$ models only, but is shown also for the CDM + Λ model for comparison purposes). Examination of these figures indicates that the radius changes in a way qualitatively similar to that found for standard CDM with an $\sim$40% decline in radius from redshift zero to a lookback of redshift $z = 0.5$. But there is an overall difference in that the radii are smaller in the CDM + Λ model. The difference, while small (-23%), is significant, especially since the lower bound produced by our finite numerical resolution is less than a factor of 2 below the mean value. Since real, observed clusters are smaller than the computed clusters, this change is also in the desired direction. The differences between the two models are

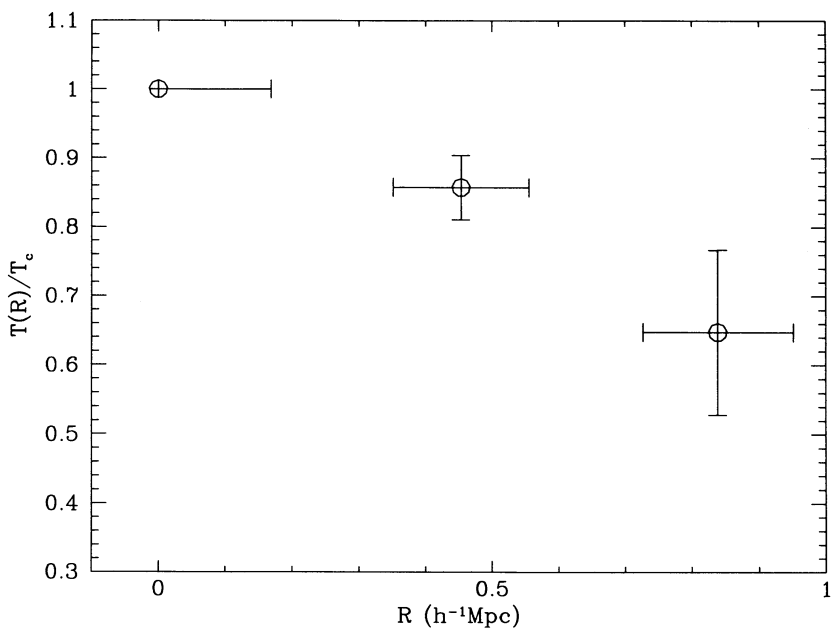

FIG. 10.—We compare the (luminosity-weighted) temperatures found in the three regions (central cell, the shell surrounding the central, and the next outer shell) and normalized to the temperature in the central cell. Departure from isothermality increase significantly for $hr > 0.5$ Mpc. Note the error bars are 1 σ variance.

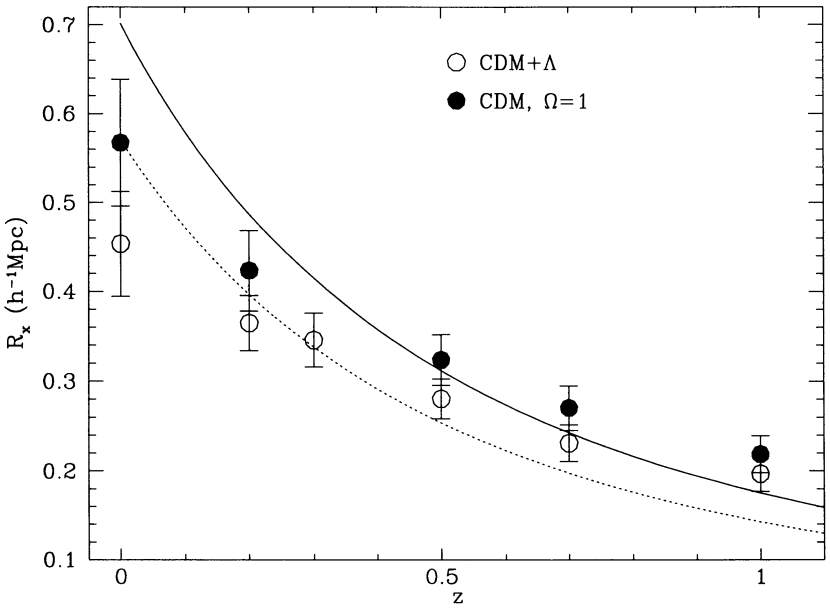

FIG. 11.—The average cluster core radii in physical units as a function of redshift for clusters with luminosity in the 0.5–4.5 keV band greater than 10^{43} ergs s^{-1} for CDM + Λ model (*open circles*; this paper) and the standard Ω = 1, CDM model (*solid dots*; KCOR). The best-fit evolutions of the form $T_x \propto (1 + z)^{-2}$ are shown as a *solid curve* for the CDM model and a *dotted curve* for the CDM + Λ model.

dramatic with regard to temperature. First, as noted, the mean temperature is a factor of 3.5 lower in the Ω < 1 model and the evolution is far slower (−33% to $z = 0.5$ rather than −48% for Ω = 1).

Thus we see that the differences between the two models at low redshift are significant and very important, due to freeze-out at low redshift in Ω < 1 models. This temperature evolution should be detectable even with a relatively "soft" X-ray instrument such as *ROSAT*. It will be able to discriminate between Ω = 1 models and Ω < 1 models. Furthermore, detailed and direct numerical simulations combined with more observations might provide a way to constrain Ω, or λ, or combinations of Ω and λ.

Figures 13 and 14 show the evolution in the background radiation field in two additional ways. The first shows what a comoving observer would have measured at various redshifts. But below 1 keV the results are unreliable because of both the omission of line emission and the omission of IGM absorption. The second, Figure 14, shows the fractional contribution to the background seen by an observer at $z = 0$ in several bands that

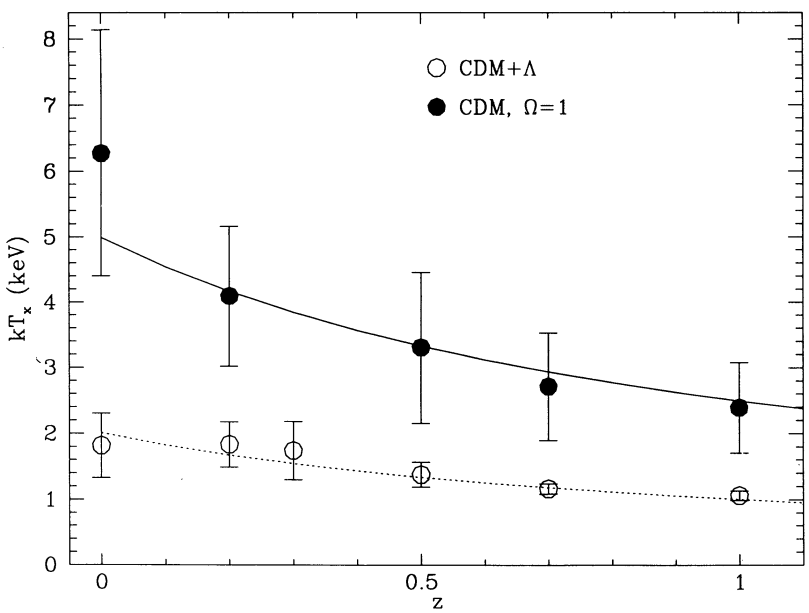

FIG. 12.—The average cluster temperature as a function of redshift for clusters with luminosity in the 0.5–4.5 keV band greater than 10^{43} ergs s^{-1} for CDM + Λ model (*open circles*; this paper) and the standard Ω = 1, CDM model (*solid dots*; KCOR). The best-fit evolutions of the form $T_x \propto (1 + z)^{-1}$ are shown as a *solid curve* for the CDM model and a *dotted curve* for the CDM + Λ model. Temperatures in the CDM + Λ model are lower and evolution less than in the standard Ω = 1, CDM model, and tend to freeze out at lower redshift while we see a dramatic increase in the CDM model approaching $z = 0$.

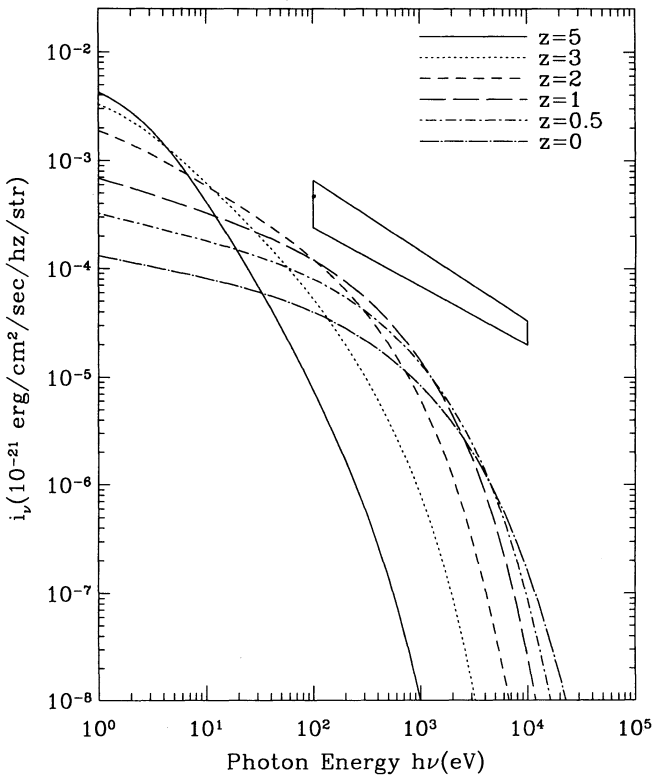

FIG. 13.—The mean radiation intensity at six epochs, $z = 5$ (*solid line*), $z = 3$ (*dotted line*), $z = 2$ (*short–dashed line*), $z = 1$ (*long–dashed line*), $z = 0.5$ (*dotted-short-dashed line*), and $z = 0$ (*dotted–long-dashed line*). The box in the middle shows the observational data by Wu et al. (1991). Neither line absorption nor emission has been allowed for in this figure.

were produced at various epochs (in integral form). The important point to note is that most of the X-ray background (especially in the harder bands) that we see locally were produced at relatively recent ($z \leq 0.5$) epochs. This is a consequence of many things, prominant among them are the redshift factors that dilute the observable effects of emission at high redshift. But there is a major difference between the two models. In this model, one-half of the 2–10 keV brightness of the sky comes from redshift less than $z = 0.3$, whereas, in the $\Omega = 1$ case (KCOR), the median point is much closer, at redshift $z = 0.2$.

Finally, let us take a slightly different route to address the issue of bias of gas relative to the mass: does the gas in dense regions, like clusters of galaxies, fairly represent the underlying mass, or is it "biased" or antibiased? This is a question with great cosmological significance. If we know the ratio of gas (+ galaxies) to total matter in the clusters by direct observations, and we know, from light element nucleosynthesis the global baryon density, then we can divide the second number by the first to obtain the global matter density and to compare with the cherished critical density. This old line of argument has been carefully reexamined recently by White (1992) and also reanalyzed by Babul & Katz (1993) and others.

The argument depends on knowing whether or not ρ_b/ρ_{tot} varies significantly from place to place and, in particular, whether this quantity will be found near its average value in the high-density regions, where it can most easily be measured.

Our possibly counterintuitive results are shown in Figure 15, where we plot the ratio (ρ_{IGM}/ρ_{tot}) versus $(\rho_{tot}/\langle\rho_{tot}\rangle)$ smoothed by a Gaussian of radius 1 h^{-1} Mpc. At any value for the total density, there is a wide range of possible values of ρ_{IGM}, but the high-density regions actually have a *lower* than average ratio of baryons to total mass. We see that, in the high-density clusters, where $\rho_{tot}/\langle\rho_{tot}\rangle$ approaches 10^3, the gas is under represented by a factor of 1.1. (In KCOR we found a factor of 1.7 for the CDM model.) Combining this factor with its global mean, we obtain that $(\rho_{gas}/\rho_{tot})_{cl} = 0.083 \pm 0.007$, which is consistent with observations $[(\rho_{gas}/\rho_{tot})_{obs} = 0.097 \pm 0.019$ for the Coma cluster for the given value of h; cf. White 1991].

We can use the comparison with KCOR to address the question of whether or not the small antibias found is real or due merely to numerical errors spreading out the gas density more than it does the dark matter density. In this simulation

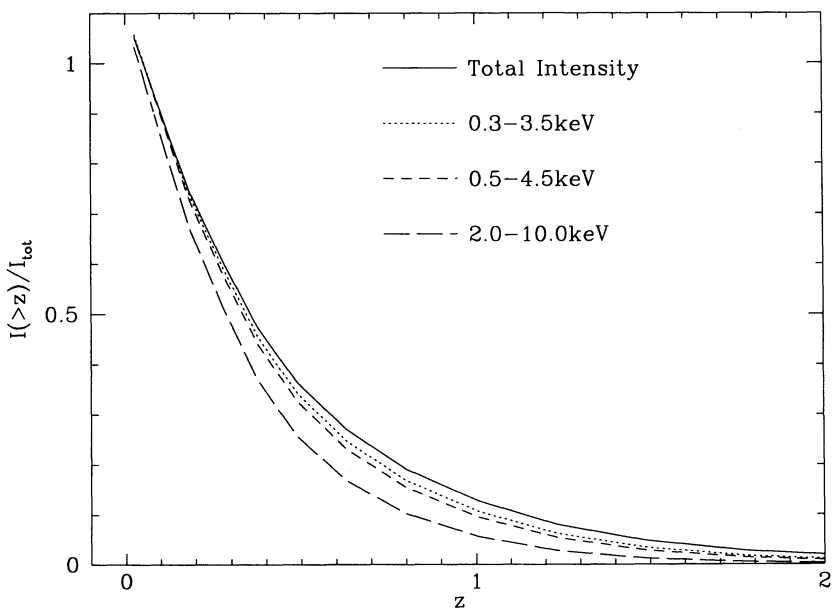

FIG. 14.—The distribution functions of four presently observed X-ray bands as a function of redshift (in integral form).

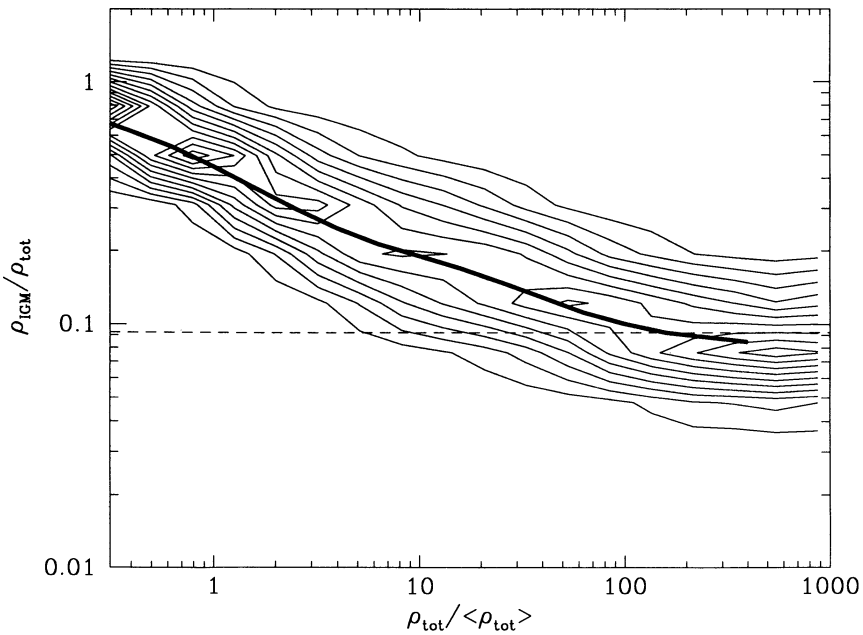

FIG. 15.—The ratio ρ_{IGM}/ρ_{tot} as a function of $\rho_{tot}/\langle\rho_{tot}\rangle$. Results are smoothed by a Gaussian window of radius 1 h^{-1} Mpc. The global mean value of $\rho_{IGM/\rho_{tot}}$ is shown by the dashed line. Note that in the highest density regions the gas is underrepresented, "antibiased," by a factor of ~1.1 (which is less than 1.7, found for $\Omega = 1$ CDM model in KCOR.

the core radii of the clusters are smaller on average than in the $\Omega = 1$ case, putting them in better agreement with observations but, as noted, closer to our grid spacing. Thus numerical diffusion in this case should be a larger (relative) effect here than in KCOR, and the antibias, if it were due to numerical diffusion, would be larger. But it is smaller, indicating that this is not the case. Our best guess is that the cause of the antibias is related to outward propagating shocks in the transient formation phase. Since such time-dependent effects will be less in open models, the antibias should be less here—as it is.

Now, we treat the same problem in a somewhat different way concentrating on the identified clusters. For each simulated X-ray cluster, we compute the gas mass and total mass within a sphere of radius 1 h^{-1} Mpc (centred at the X-ray cluster center) and in Figure 16 we show the ratio (open circles) of the two masses within this sphere as a function of density of the sphere relative to the mean. The dotted line is the best log-log straight line fit for the open circles, and the solid line is the fit weighted by the luminosity of each cluster. Also shown, as the dashed line, is the global mean of the ratio. Presenting the same information in an alternative way, we show in Figure 17 the histogram of the ratio, both number-weighted (thin solid histogram) and luminosity-weighted (thin dotted histogram) in the CDM + Λ model. The heavy solid histogram (arbitrarily normalized to have a similar peak height) indicating the observational situation is adopted from Jones & Forman (1992). We see that there is a trend that poor clusters are relatively gas poor, which is consistent with observations (cf., e.g., Jones & Forman 1992). The luminosity-weighted fit is closer to (but still below) the global mean with an antibias in the range 0.85–0.92. We see that the median of the computed ratio is in agreement with the median of the observed ratio, whereas in the CDM $\Omega = 1$ model the computed ratio is lower by a factor of 2–3. Improving the observations will probably narrow the heavy histogram, and increasing the dynamical range of our simulation box will widen the thin histograms. Both expected improvements should make the agreement better.

4. CONCLUSIONS

In Figures 1–5 we show the evolution of the cluster lumnosity function expected in the CDM + Λ model. In the range of parameters where there is greatest overlap between observed and computed quantities ($0 \leq z \leq 1$, 10^{40} ergs $s^{-1} \leq L_x \leq 10^{44}$ ergs s^{-1}), little evolution is seen (for comoving observers) in any of the computed bands aside from a decline in the number of brightest sources (somewhat uncertain due to our limited box size) and a modest increase (by about a factor of 2) in the luminosity function for fainter objects. A similar behavior was also found in the CDM model (KCOR). But the likely explanation for this is different from that in the CDM case. While in the standard CDM model, it is largely coincidental and due to the balancing of two effects: new breaking waves increase the luminosity density but mergers decrease it. In this CDM + Λ model it is primarily due to the late-time freeze-out of formed clusters. The effect is seen most clearly in Figure 5, where we look only at the evolution of the brightest clusters, and see an earlier decline (with increasing redshift) of the $\Omega < 1$ model than the $\Omega = 1$ models. There is an order of magnitude decline in the number density of clusters having $L_x > 10^{43}$ ergs s^{-1} (in the harder energy bands) in the redshift interval $z = 0 \rightarrow 2$ for this model but an increase in the standard $\Omega = 1$ CDM model. The strong negative evolution found in this paper in a $\Omega < 1$ model would of course be greatly enhanced for observers (using fixed bands and intensity limits) by cosmological effects which are especially strong in models with a cosmological constant (Carroll, Press, & Turner 1992).

Figures 6 and 7 show rates of change in other quantities, the temperatures and clusters radii. These important trends are summarized in Figures 11 and 12 where we see a factor of 2–3 decline in both these quantities by redshift 1. But more inter-

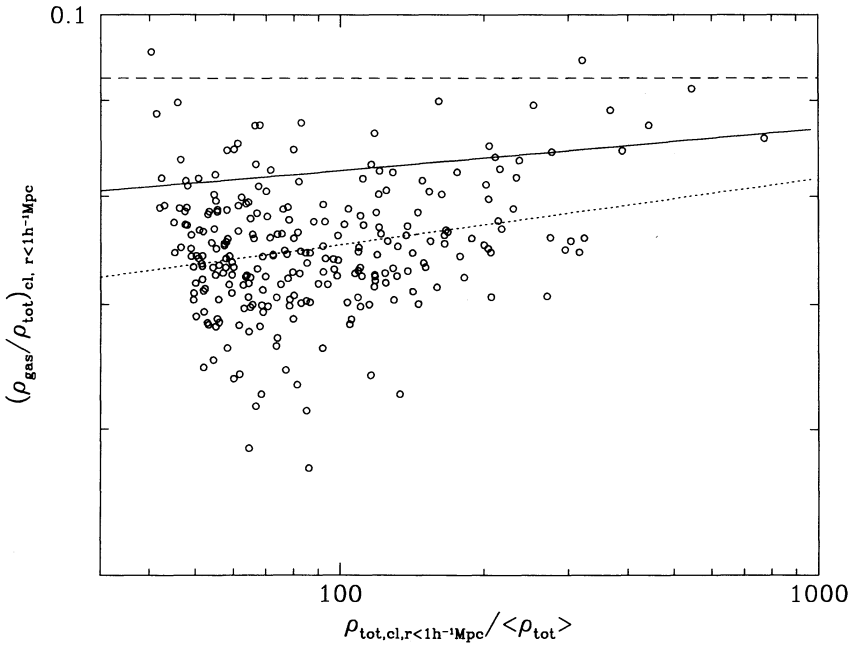

FIG. 16.—The ratio ρ_{gas}/ρ_{tot} as a function of $\rho_{tot}/\langle\rho_{tot}\rangle$ within a radius of 1 h^{-1} Mpc for each identified cluster (*open circles*). The *dotted line* is the best log-log straight line fit for the *open circles*, and the *solid line* is the fit weighted by the luminosity of each cluster. Also shown as the *dashed line* is the global mean of the ratio. We see that there is a trend that poor clusters are relatively gas poor.

esting is the nearly constant mean temperature (luminosity-weighted) in the redshift range $z = 0 \rightarrow 0.3$ in the CDM + Λ while in the CDM model we see a sharp decrease in the temperature from $z = 0.0$ to $z = 0.3$. Equivalently put, L^* of Schechter fits to the computed luminosity functions peaks near $z = 0.3$ in the CDM + A model but it increases monotonically until $z = 0$ in the CDM model. Both trends should be detectable even with a relatively "soft" X-ray instrument such as *ROSAT*. They might provide powerful tests for $\Omega = 1$ models and $\Omega < 1$ models. Also the actual values of the cluster temperature are much lower in this model and in better agreement with observations.

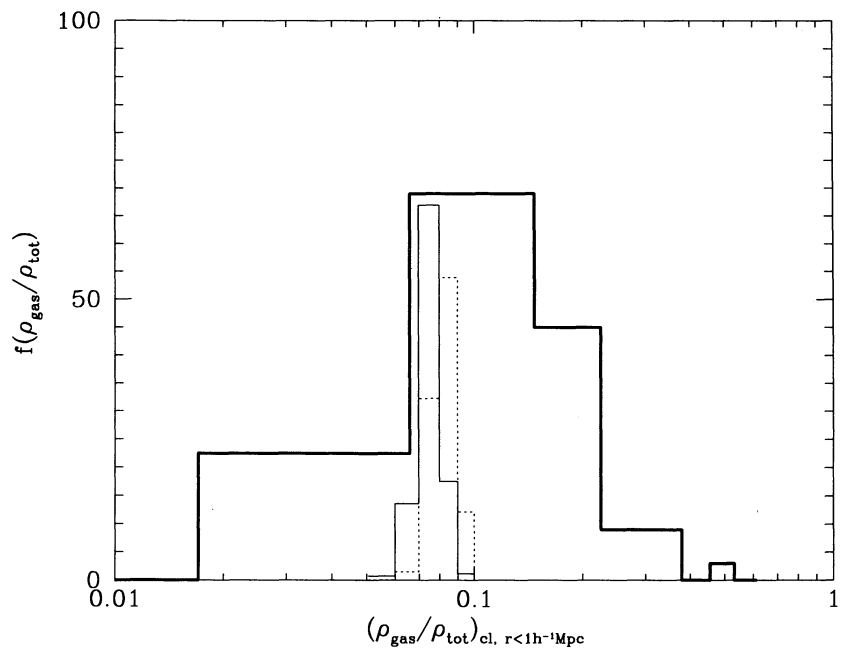

FIG. 17.—The histogram of the ratio both number-weighted (*thin solid histogram*) and luminosity-weighted (*thin dotted histogram*) in the CDM + Λ model. The *heavy solid histogram* indicating the observational situation is adapted from Jones & Forman (1992). We see that there is a trend that poor clusters are relatively gas poor, which is consistent with observations (cf., e.g., Jones & Forman 1992). The luminosity-weighted fit is closer to (but still below) the global mean, with an antibias in the range 0.85–0.92. We see that the median of the computed ratio is in agreement with the median of the observed ratio, whereas in the CDM $\Omega = 1$ model the computed ratio is lower by a factor of 2–3. Improving the observations will probably narrow the heavy histogram, and increasing the dynamical range of our simulation box will widen the thin histograms. Both expected improvements should make the agreement bettter.

This CDM + Λ model provides an adequate fit to the observed bright X-ray cluster luminosity function and X-ray background; however, we found that there would be too many bright X-ray clusters produced and too much integrated background X-ray intensity in the *COBE*-normalized standard CDM model.

We find a slight antibias ($\sim 10\%$) of gas relative to the mass in dense regions like the clusters of galaxies, but the model is self-consistent in the sense that the computed $(\rho_{\rm gas}/\rho_{\rm tot})_{\rm cl}$ $(= 0.083 \pm 0.007)$ is consistent with observations $[(\rho_{\rm gas}/\rho_{\rm tot})_{\rm obs} = 0.097 \pm 0.019$ for the Coma cluster for the given value of h, cf. White 1991], whereas there was a gross inconsistency in the $\Omega = 1$ case.

In sum, the model is significantly different from that obtained from the standard $\Omega = 1$, CDM simulation, and, with regard to all measurable quantities that we have compared to observations $[N(L_x)$, $\langle R_x \rangle$, $\langle T_x \rangle$, $d \ln T_x / d \ln L_x$, $\rho_{\rm gas}/\rho_{\rm tot}]$, it is not only a better fit to observations than standard $\Omega = 1$, CDM model, but also is an adequate representation of them. The predicted evolutionary differences between $\Omega < 1$ and $\Omega = 1$ models are sufficiently greater to allow definitive tests by current or planned X-ray satellite observations.

We are happy to acknowledge support from NASA grant NAGW-2448, NSF grant AST91-08103 and the NSF HPCC grant ASC93-18185. We would like to especially thank R. Reddy for his valuable help and patient effort to optimize the code on the Cray-YMP C90 supercomputer. It is a pleasure to acknowledge the Pittsburgh Supercomputer Center for allowing us to use their Cray-90 and the help of Koushik Ghosh from Cray Research on the FFT routines. Discussions with N. Gnedin, P. Henry, and S. White are gratefully acknowledged.

REFERENCES

Babul, A., & Katz, N. 1993, ApJ, 406, L251
Bryan, G. L., Cen, R. Y., Norman, M. L., Ostriker, J. P., & Stone, J. M. 1994, ApJ, in press
Carroll, S. M., Press, W. H., & Turner, E. L. 1992, ARA&A, 30, 499
Cen, R. Y. 1992, ApJS, 78, 341
Cen, R. Y., Gnedin, N. Y., & Ostriker, J. P. 1993, ApJ, 417, 387
Cen, R. Y., & Ostriker, J. P. 1992, ApJ, 399, L113
———. 1993, ApJ, 417, 415
Efstathiou, G. 1993, Proc. National Acad. of Sciences, Vol. 90, No. 11, Galaxy Clustering on Large Scales, 693, 4859
Estathiou, G., Bond, J. R., & White, S. D. M. 1992, MNRAS, 258, 1P
Henry, J. P. 1992, in Clusters and Superclusters of Galaxies, ed. A. C. Fabian (Dordrecht: Kluwer), 311
Henry, J. P., & Arnaud, K. A. 1991, ApJ, 372, 410
Jones, C., & Forman, W. 1992, in Clusters and Superclusters of Galaxies, ed. A. C. Fabian (Dordrecht: Kluwer), 49
Kaiser, N. 1986, MNRAS, 222, 323
Kang, H., Cen, R. Y., Ostriker, J. P., & Ryu, D. 1994, ApJ, in press (KCOR)
Kofman, L. A., Gnedin, N. Y., & Bahcall, N. A. 1993, ApJ, 413, 1
Ostriker, J. P. 1993, ARA&A, 31, 689
Ryu, D., Ostriker, J. P., Kang, H., & Cen, R. Y. 1993, ApJ, 414, 1
Walker, T. P., Steigman, G., Schramm, D. N., Olive, K. A., & Kang, H. S. 1990, ApJ, 376, 51
White, S. D. M. 1992, in Clusters and Superclusters of Galaxies (Dordrecht: Kluwer), 17
Wu, X., Hamilton, T., Helfand, D. J., & Wang, Q. 1991, ApJ, 379, 564